# Design of a Near Field Protective Dielectric Radome "Window" for a Curved Phased Array Antenna-Axial Polarization Case

## A. E. Fathy

The University of Tennessee, EECS Department, Knoxville, TN 37996-2

*Abstract* − A systematic design method of near field dielectric windows for 2D conformal fed arrays was previously developed. This developed design yielded simultaneously well-behaved element patterns in both axial and circumferential polarization. The method includes dimensioning of the window thickness to maximize the radial decay rate of the radome induced surface waves, followed by inclusion of a sufficiently large gap to decouple the surface waves from the array face. This methodology has been successfully extended to 3D with circumferential polarization according to the previously established guidelines and has provided smooth patterns in the circumferential plane, but limited the scan in the axial plane. Here we will investigate the case with axial polarization and compare the available useful scan volume to that of circumferentially polarized excitation.

## I. INTRODUCTION

The suitability of a near field protective dielectric radome for a curved phased array antenna has been judged by the acceptability of the element patterns in the presence of the radome [1]. Such a dielectric radome in the near field of a curved phased array antenna may cause significant deterioration of the element pattern, which manifests itself in pronounced dips (10-20 dB) and a large ripple off broadside in the element pattern. These undesirable effects are due to guided waves induced by the radome [1].

A practical approach to reduce these effects is to separate the radome somewhat from the radiating elements and adjust the air gap to produce a compensating effect which smoothes out the element pattern [1]. This method has been extended to evaluate a systematic design method of shaping the element patterns in the presence of a near field radome by adjusting the radome thickness, and the distance of the radome from the array elements in order to smooth out the element patterns [1, 2]. This method is particularly relevant to protective dielectric windows for missile phased arrays [3-5].

This approach has been extended for 3D structures for the circumferential polarization case in [2]. Direct evaluation of the element patterns for the 3D-optimized window geometries, and the results have indicated that a significant reduction of guided wave effects is possible. The elements spacing is not smaller than 0.5 λ, and the compensation is accomplished by an adjustable air gap as

well. By appropriately designing the radome [6], it was possible to scan a phased array beam efficiently in the E-plane (circumferential plane), but the cost is the appearance of a blind spot caused by the presence of the air gap, which limits the H-plane scan (axial-scan in this case). The location of this dip is predictable from the planar dispersion curves of a dielectric slab spaced from and parallel to a ground plane. Cross polarization is encountered off the principal planes due to polarization coupling at the dielectric-air interfaces. The amount of cross polarization increases with decreasing $\theta$, i.e. increasing elevation angle from broadside. When the near field radome is spaced away from the radiating elements, the principal polarization is still dominant in the shadow region but may be highly rippled due to the presence of low attenuation guided waves. With a proper choice of parameters, the level of the shadow region-element pattern ripple may be reduced without an excessive air gap size.

In the present paper, these ideas have been extended further to arrays scanning in the axial or near the axial-direction, when the coupling between longitudinal section electric 'LSE' and longitudinal section magnetic 'LSM' polarizations by the dielectric layer are present. The method of radome design for the axially polarized-rectangular waveguide elements is pursued here according to the guidelines established in [1] and will be compared to that of the circumferentially polarized case presented in detail in [2].

## II. ANALYSIS

The model, shown in Fig. 1, is very similar to the one used for the circumferentially polarized case [2], with one exception that the orientations of the radiating waveguides are different. Both structures are comprised of uniformly spaced infinite arrays of open-ended rectangular waveguides in a rectangular lattice embedded in a perfectly conducting circular cylindrical surface of radius ρ surrounded by a concentric lossless dielectric sleeve radome. Therefore, the formulation of the two different polarizations is very similar until we apply the boundary conditions at the surface of the conducting cylinder. Therefore, we will summarize here the main analysis steps, but for more details refer to [2].

The structure has $N$ elements in a ring and the axial inter-ring spacing is $d$. A single waveguide is excited while all others are match-terminated [3-5]. The dielectric

loaded feed waveguides solely propagate a TE$_{10}$ mode and include identical matching networks with parameters appropriate to a chosen circumferential and axial progressive element phasing (ν,ζ). A single mode waveguide aperture approximation should be sufficient to account for dominant mutual coupling effects.
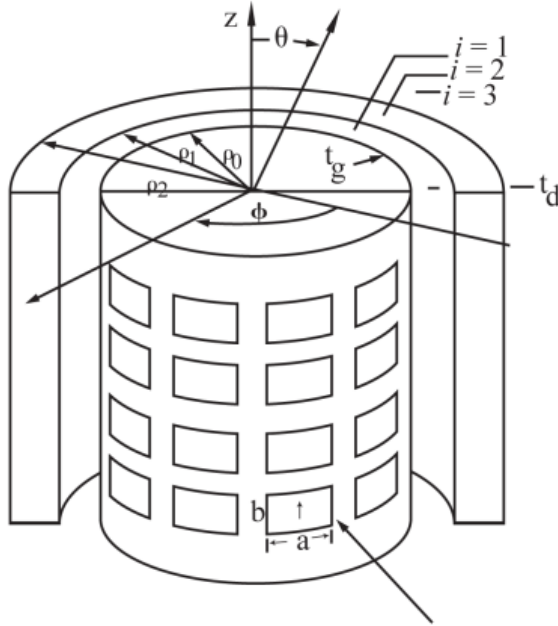


AXIAL POLARIZATION

Fig. 1. Circular Array Geometry of a dielectrically covered circular array of infinite axial slits on a large conducting cylinder.

### A. Formulation

As in the absence of the dielectric radome [2], the electric fields radiated by an element in a match-terminated cylindrical array with a concentric sleeve radome are formally given by,

$$\underline{E}(\underline{r}) = \frac{d}{2\pi N} \int_{-\frac{\pi}{d}}^{\frac{\pi}{d}} d\zeta \sum_{v=0}^{N-1} \underline{E}(r, v, \zeta) \qquad (1)$$

where $\underline{E}(\underline{r})$ is the E-field in the radial unit cell for the steering phase (ν,ζ). As for a given set of (ν,ζ), the problem reduces to determining the field radiated by a rectangular waveguide into a sectored-waveguide whose walls are characterized by "phase shift" walls.

For the sake of analysis, it is sufficient to consider only the transverse to $\rho$ field components $\underline{E}$ and $\underline{H}$, and in each radially homogeneous region, these fields can be represented in terms of a complete set of *LSM(`)* ($H_z = 0$) and *LSE(``)* ($E_z = 0$) modes.

A (m,n) *LSM or LSE* mode has the form [3],

$$\underline{E}_{v_m,\varsigma_n}^{(',")}(\underline{r}) = v_{v_m,\varsigma_n}^{(',")}(\rho) \underline{e}_{v_m,\varsigma_n}^{(',")}(\phi, z) \qquad (2)$$

$$\underline{H}_{v_m,\varsigma_n}^{(',")}(\underline{r}) = i_{v_m,\varsigma_n}^{(',")}(\rho) \underline{h}_{v_m,\varsigma_n}^{(',")}(\phi, z) \,, \qquad (3)$$

$$v_m = v + mN; \qquad \varsigma_n = \varsigma + \frac{2\pi}{d}n \,, \qquad (4)$$

where

$$m, n = 0, \pm 1, \pm 2, ...$$

$i_{v_m,\varsigma_n}^{',"}$ and $v_{v_m,\varsigma_n}^{',"}$ satisfy the Bessel's differential equation (as given in Appendix A1 of [2]). Additionally, for an $e^{j\omega t}$ time dependence, the orthogonal vector mode functions are,

$$\underline{e}_{v_m,\varsigma_n}^{'} = (\frac{-v_m \varsigma_n}{\rho \kappa_n^2} \underline{\phi}_o + \underline{z}_o) e^{-j(v_m\phi + \varsigma_n z)}$$
$$(5)$$

$$\underline{h}_{v_m,\varsigma_n}^{'} = (\frac{-1}{\rho} \underline{\phi}_o) e^{-j(v_m\phi + \varsigma_n z)} \,, \qquad (6)$$

and

$$\underline{e}_{v_m,\varsigma_n}^{"} = (\frac{1}{\rho \kappa_n^2} \underline{\phi}_o) e^{-j(v_m\phi + \varsigma_n z)} \,, \qquad (7)$$

$$\underline{h}_{v_m,\varsigma_n}^{"} = (\frac{-v_m \varsigma_n}{\rho \kappa_n^2} \underline{\phi}_0 + z_o) e^{-j(v_m\phi + \varsigma_n z)} \,, \qquad (8)$$

where $(\underline{\rho}_o, \underline{\phi}_o, \underline{z}_o)$ are the cylindrical unit vectors.

Upon utilizing the following representations,

$$V_{v_m,\varsigma_n}^{'} = v_{v_m,\varsigma_n}^{'}; \qquad V_{v_m,\varsigma_n}^{"} = v_{v_m,\varsigma_n}^{"} / \rho \qquad (9)$$

$$I_{v_m,\varsigma_n}^{'} = i_{v_m,\varsigma_n}^{'} / \rho; \qquad I_{v_m,\varsigma_n}^{"} = i_{v_m,\varsigma_n}^{"}. \qquad (10)$$

Expressions for the radial modal transmission line in the i$^{th}$ layer (see Fig. 1) are given in Appendix A.

Both the total voltage $V_{v_m,\varsigma_n}^{(",')}(\rho)$ and the total current $I_{v_m,\varsigma_n}^{(",')}(\rho)$ at any radial distance $\rho$ or the forward-traveling (+) and backward-traveling (-) voltages and currents given by $V_{v_m,\varsigma_n}^{(",')(\pm i)}$ and $I_{v_m,\varsigma_n}^{(",')(\pm i)}$ will be expressed in terms of V$_o$(ν,ζ), and $I_o(v,\varsigma)$ as shown in section III. Wherein V$_o$(ν,ζ) and I$_o$(ν,ζ) are the dominant feed waveguide voltage and current just below the feed aperture.

In our analysis, the total voltages and currents at the cylindrical conducting surface given by $V_{v_m,\varsigma_n}^{"}(\rho_o^+)$, $V_{v_m,\varsigma_n}^{'}(\rho_o^+)$, $I_{v_m,\varsigma_n}^{"}(\rho_o^+)$, and $I_{v_m,\varsigma_n}^{'}(\rho_o^+)$ are related to the forward-traveling waves in the exterior region (i.e.in

layer i=3) given by the unknowns $I_{v_m,\zeta_n}^{''(+3)}$ and $V_{v_m,\zeta_n}^{'(+3)}$. This relationship is determined by using the boundary conditions at the various air-dielectric interfaces at $\rho_1$ and $\rho_2$, the transmission of both the LSM and LSE modes across the two layers i.e. i=1 and i=2, and the radiation condition at $\rho \rightarrow \infty$. The various mode transmission and coupling through the two dielectric layers and their associated coupling at the air-dielectric interfaces at $\rho_1$ and $\rho_2$ are expressed by an overall transmission matrix $T_{12}$ as shown by equation (11), and the $T_{12}$ matrix elements are given in Appendix B,

$$\begin{bmatrix} V_{v_m,\zeta_n}^{''}(\rho_o^+) \\ I_{v_m,\zeta_n}^{''}(\rho_o^+) \\ V_{v_m,\zeta_n}^{'}(\rho_o^+) \\ I_{v_m,\zeta_n}^{'}(\rho_o^+) \end{bmatrix} = T_{12} \begin{bmatrix} I_{v_m,\zeta_n}^{''(+3)} Z_{n3}^{''} H_{v_m}^{(2)'}(\kappa_{n3}\rho_2) \\ I_{v_m,\zeta_n}^{''(+3)} H_{v_m}^{(2)}(\kappa_{n3}\rho_2) \\ V_{v_m,\zeta_n}^{'(+3)} H_{v_m}^{(2)}(\kappa_{n3}\rho_2) \\ V_{v_m,\zeta_n}^{'(+3)} Y_{n3}^{'} H_{v_m}^{(2)'}(\kappa_{n3}\rho_2) \end{bmatrix} \quad (11)$$

where expressions for $Z_{n3}^{''}$ and $Y_{n3}^{'}$ are given in Appendix A, and $H_n^{(1,2)}(x)$ is Hankel function of order n, type 1 or 2, and argument x .

## III. ACTIVE ADMITTANCE FOR AXIAL POLARIZATION

The single mode aperture approximation, for an axially polarized feed waveguide aperture, requires that in the unit cell,

$$E_{\phi_{v_m,\zeta_n}}(\rho_o) = 0 . \quad (11)$$

Therefore equations (2) and (10) imply,

$$V_{v_m,\zeta_n}^{''}(\rho_o^+) = \frac{\zeta_n v_m}{\kappa_{n1}^2 \rho_o} V_{v_m,\zeta_n}^{'}(\rho_o^+) . \quad (12)$$

Matching the tangential field components, assuming that the aperture is only slightly curved, the single mode aperture approximation requires that the following relations to be satisfied in the Galerkin's sense,

$$\sum_{m,n} V_{v_m,\zeta_n}^{'}(\rho_o)e^{-j(v_m\phi+\zeta_n z)}$$

$$\begin{cases} = \sqrt{\frac{2}{ab}} V_o(v,\zeta)\sin\frac{\pi}{2}(\rho_o\phi+a/2) \quad on \quad S_f \\ = 0 \quad elsewhere \ the \ unit \ cell \end{cases} \quad (13)$$

$$\sum_{m,n}[-I_{v_m,\zeta_n}^{'}(\rho_o) - (\frac{\zeta_n v_m}{\kappa_{n1}^2 \rho_o})I_{v_m,\zeta_n}^{''}(\rho_o)] =$$

$$-\sqrt{\frac{2}{ab}}I_o(v,\zeta)\sin\frac{\pi}{2}(\rho_o\phi+a/2) \quad on \quad S_f \quad (14)$$

where $S_f$ is the feed guide aperture, and $V_o(v,\zeta)$ and $I_o(v,\zeta)$ are the TE$_{10}$ modal voltage and current respectively.

Employing Galerkin's procedure, one has, from equation (14),

$$V_{v_m,\zeta_n}^{'}(\rho_o) = \frac{\alpha^{'}(v,\zeta)}{\rho_o\beta d}V_o(v_m,\zeta_n) \quad (15)$$

where

$$\alpha^{'}(v_m,\zeta_n) =$$

$$\sqrt{\frac{2}{ab}}\int_{S_f}\sin\frac{\pi}{a}(\rho\phi+a/2)e^{+j(v_m\phi+\zeta_n z)}\rho d\phi dz , \quad (16)$$

$$= \frac{2ab}{\pi}\sqrt{\frac{2}{ab}}\frac{\sin(\frac{\zeta_n b}{2})}{\frac{\zeta_n b}{2}}\frac{\frac{\pi^2}{4}\cos(\frac{v_m a}{2\rho_o})}{\frac{\pi^2}{4}-(\frac{v_m a}{2\rho_o})^2}$$

and

$$\beta = 2\pi/N, \quad (17)$$

also, equation (15) yields,

$$I_o(v,\zeta) =$$

$$\sum_{m,n}[I_{v_m,\zeta_n}^{'}(\rho_o^+) + (\frac{\zeta_n v_m}{\kappa_{n1}^2 \rho_o})I_{v_m,\zeta_n}^{''}(\rho_o^+)]\alpha^{'}(v_m,\zeta_n) . \quad (18)$$

Upon expressing $I_{v_m,\zeta_n}^{''}(\rho_o)$ and $I_{v_m,\zeta_n}^{'}(\rho_o)$ as functions of $V_o(v,\zeta)$, we finally can find the ratio of $I_o(v,\zeta)/V_o(v,\zeta)$ which is the active admittance $Y_a(v,\zeta)$.

### A. Active Reflection Coefficient

To maximize the broadside element gain and preserve the circular symmetry of the array, identical networks are included in all feed waveguides to match the array for in phase excitation of all elements (v=0, $\zeta$=0), where the active reflection coefficient $\Gamma_a(v,\zeta)$.at the input to the matching network is,

$$\Gamma_a(v,\zeta) = \frac{(Y_a(0,0) - Y_a(v,\zeta))}{(Y_a^*(0,0) + Y_a(v,\zeta))} . \quad (19)$$

From the equivalent network of Fig. 2, it is apparent that for the $(\nu,\zeta)$ excitation, the $TE_{10}$ modal voltage $V_o(\nu,\zeta)$ at the aperture is related to the incident voltage $V^{inc}$ and is given by,

$$V_o(\nu,\zeta) = V^{inc}\tilde{n}(1+\Gamma_a(\nu,\zeta))$$

$$= V^{inc}\tilde{n}T(\nu,\zeta) = V^{inc}\tilde{n}\frac{2G_a(0,0)}{Y_a^*(0,0)+Y_a(\nu,\zeta)} \quad (20)$$

with

$$Y_a(\nu,\zeta) = G_a(\nu,\zeta) + jB_a(\nu,\zeta)$$

and $\tilde{n} = \sqrt{\dfrac{Y_o}{G_a(0,0)}}$

where $Y_o$ is the admittance of the $TE_{10}$ feed waveguide mode.
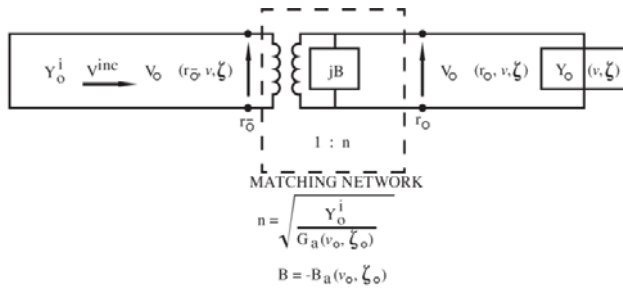


Fig. 2. The matching network.

### B. Element Pattern

The exterior unit cell voltages $V''_{\nu_m,\zeta_n}(\rho_2^+)$ and $V'_{\nu_m,\zeta_n}(\rho_2^+)$ are calculated in terms of $V^{inc}$ upon utilizing Appendix C and equation (20).

The expression for the far field of a singly excited element in a mutually coupled environment is given by [2],

$$\underline{E}(\underline{r}) =$$
$$\frac{d}{N}(\frac{e^{-jk_o r}}{r})V^{inc}\tilde{n}\sum_{\nu=-\infty}^{\infty}T(\nu,k\cos\theta)e^{-j\nu(\phi-\pi/2)}\underline{A}(\nu,\theta) \quad (21)$$

where

$$\underline{A}(\nu,\theta) = [\frac{jV''_{\nu,k\cos\theta}(\rho_2^+)\rho_o}{V_o(\nu,k\cos\theta)H_\nu^{'(2)}(k_o\rho_2\sin\theta)}\underline{\phi_o}$$

$$+\frac{V'_{\nu,k\cos\theta}(\rho_2^+)}{V_o(\nu,k\cos\theta)\sin\theta}\frac{}{H_\nu^{(2)}(k_o\rho_2\sin\theta)}\underline{\theta_o}] \quad (22)$$

with

$$V_o(\nu,k\cos\theta) = \tilde{n}T(\nu,k\cos\theta)V^{inc} \quad (23)$$

Equations (21-23) are formally valid for both polarizations, provided appropriate expressions for $V''_{\nu,k\cos\theta}/V_o$, and $V'_{\nu,k\cos\theta}/V_o$ are used. For the axial polarization these are numerically obtained using Appendix C.

### C. Element Gain Amplitude

The total element power gain is given by,

$$G = 4\pi\frac{r^2}{|V^{inc}|^2 Y_o}\frac{|E|^2}{\eta_o} = G_\theta^2 + G_\phi^2 \quad (24)$$

where $\eta_o=120\pi$ ohms and $G_\phi$ and $F_\phi$ are given by,

$$G_\theta = \frac{4\pi dc}{\lambda^2}\frac{|F_\theta(\theta,\phi)|^2}{\pi k_o r_o\sqrt{\dfrac{G_a'(o,o)}{\eta_o}}} = \frac{4\pi dc}{\lambda^2}g_\theta^2 \quad (25)$$

$$F_\theta(\theta,\phi) = \sum_{\nu=-\infty}^{\infty}T(\nu,k\cos\theta)\underline{A}_\theta e^{-j\nu(\phi-\pi/2)} \quad (26)$$

where

$$G_a'(0,0) = \text{Re}[Y_a(0,0)]\frac{\pi^2 cd}{8ab}. \quad (27)$$

Similar expressions can be derived for the circumferential components such as cross-polarization upon replacing $\theta$ by $\phi$ in equation (26).

## IV. NUMERICAL RESULTS AND DISCUSSION

The numerical results for rectangular waveguide cylindrical array element patterns in the presence of a near field dielectric radome (window) are presented for nominally axial element polarization. These results stress the aspects relevant to blind spot free, conformal near field radomes. They indicate a significant influence of guided waves and illustrate the extent of validity of the design method of [l] for dielectric windows to reduce these deleterious effects. In addition to the guided wave effects, the polarization aspects of the element pattern as influenced by the curvature and the presence of the radome are considered.

As in the two and 3D dimensional arrays of [l, 2], the element amplitude patterns are presented for representative values of array parameters and the results are grouped in such a way to exhibit the significant trends.

## A. Effect of Gap Size

Figures 3-13 present element patterns ($k_o\rho_o = 50$, a/$\lambda$ = 0.435, b/$\lambda$ = 0.2, c/$\lambda$ = d/$\lambda$ = 0.5) for waveguides oriented so as to produce axial polarization as shown in Fig. 1. The dielectric constant is $\varepsilon_r = 2.56$ unless otherwise stated.

In all cases the field (voltage) element patterns were normalized to the unit cell gain $\sqrt{4\pi dc \,/\, \lambda^2}$, and a single mode aperture approximation was used. The numerical results stress the element gain pattern-aspects that are relevant to the blindspot-free conformal array design.

An extremely close similarity has been found between the normalized gain pattern in the $\theta=90°$ cut and the H-plane patterns in the two-dimensional arrays with a similar geometry. Therefore, in order to save computer time, we have replaced, unless otherwise stated, the $\theta=90°$ H-plane cuts by the 2-D results [1]. When the dielectric window overlays the array face ($t_g = 0$), and $t_d/\lambda = 0.2$, the H-plane element pattern (see Fig. 3) does not exhibit blindspots, but is slightly rippled, which might be acceptable. However, the element pattern deteriorates with $\theta$ off the principal H-plane. The large ripple is due to the coupling to the cross-polarized guided waves, which are absent for $\theta = 90°$.

In order to reduce this effect, an air gap is introduced, and Fig. 3 shows different situations arising as the air gap is increased. Consider first the $\theta = 90°$ (H)-plane case, where it is initially seen that the patterns deteriorate and blindspot dips appear upon introducing the air gap (see the two cases $t_g/\lambda$ = 0.25 and 0.4). However for $t_g/\lambda$ = 0.5 at the $\theta = 90°$, the pattern already becomes very smooth because of the surface wave decoupling. In order to facilitate understanding of the main features of the $\theta = 90°$ (i.e. H-plane) element pattern with the inclusion of an air gap, the assumption of the validity of the planar approximation will be adopted, as in the 2-D case.

To exhibit the element pattern for small departures from the $\theta = 90°$ cut, Fig. 6 shows conical cuts of $\theta = 85°$ for $t_g/\lambda$ = 0.2, 0.4 and 0.5 which exhibit only minor changes from the respective $\theta = 90°$ patterns, meanwhile the cross polarization level is small. Consequently, the design method is also applicable for small departures from $\theta = 90°$.

With the aid of Figs. 4 and 5 and equation (28), one may estimate the radial surface wave decoupling away from the curved dielectric sheets towards the array face. A 20dB wave decoupling was calculated to be 20 dB for $t_g/\lambda$ = 0.5; which is seen to be sufficient for $k_o\rho_o = 50$.

Continuing further, for $\theta = 60°$ (Figs. 7 and 8), the gain drops with decreasing values of $\theta$, but for $t_g/\lambda$ = 0.5 we have already a smooth element pattern in the principal polarization. However, as expected, the amount of cross-polarization increases.

Figure 9 shows smooth element patterns for the $\theta = 45°$ in the case of $t_d/\lambda$ = 0.2 and $t_g/\lambda$ = 0.5. Thus, the design method applies here, as well, but it is not possible to scan much beyond $\theta = 45°$,
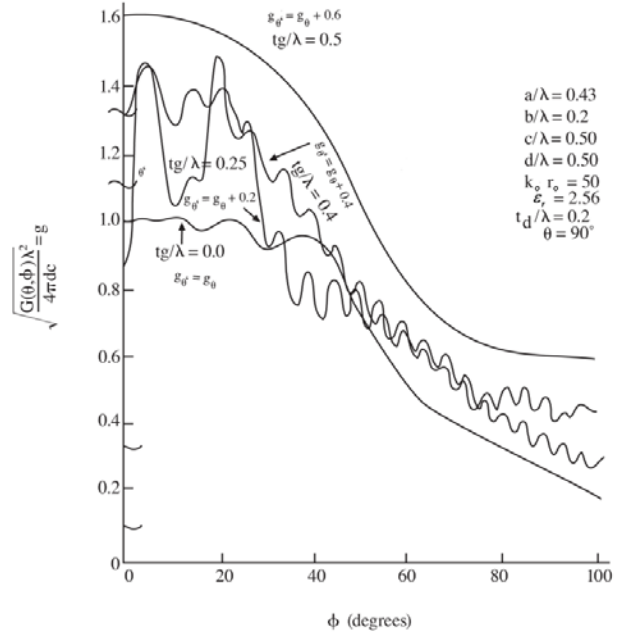


Fig. 3. Effect of air gap size "$t_g/\lambda$" on element gain patterns for different gap sizes ($t_g/\lambda$=0, 0.2, 0.4, and 0.5) for $k_o r_o$=50, a/$\lambda$=0.43, b/$\lambda$=0.2, d/$\lambda$=0.5, $t_d/\lambda$=0.2, $\varepsilon_r$=2.56, for $\theta$=90° cuts. Patterns were combined in one figure, and for easy comparison, we added a 0.2 for $t_g/\lambda$=0.25 gain case, a 0.4 for the $t_g/\lambda$=0.4 case, and a 0.6 for the $t_g/\lambda$=0.5 case to separate their respective performances.
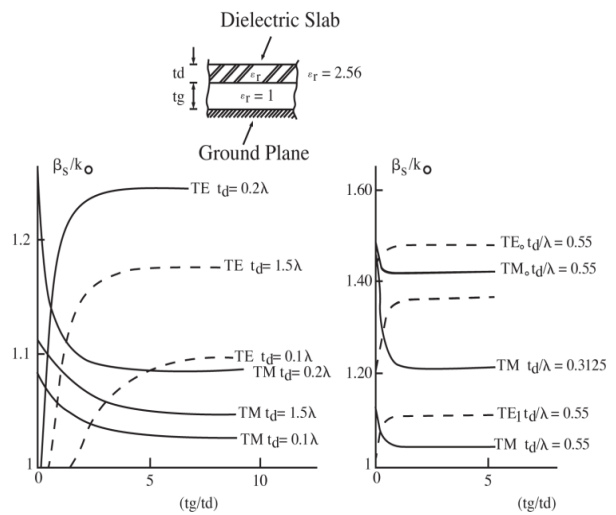


Fig. 4a. Effect of air gap size on surface wave propagation for $\varepsilon_r$=2.56.
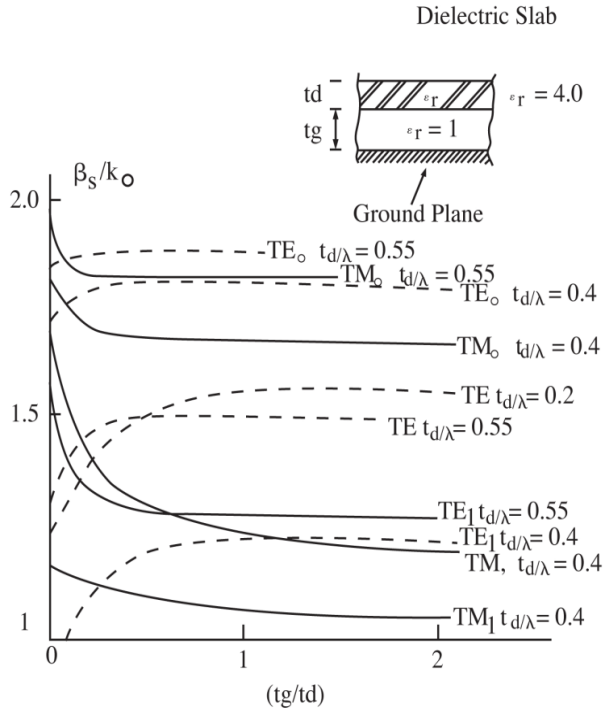
Fig. 4b. Effect of air gap size on surface wave propagation for $\varepsilon_r=4$.

Because of the E-plane dip at $\theta = 32°$ (from the axis), as predicted from Figs. (4, 5) and from the condition (28) for a blindspot in a planar array.
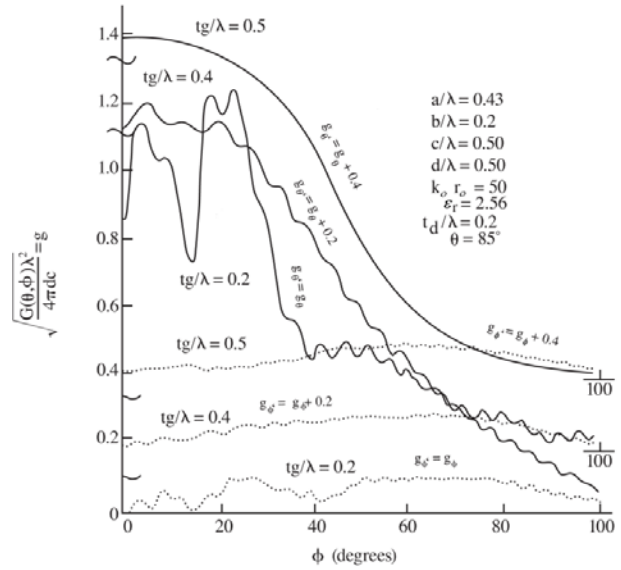


Fig. 6. Effect of air gap size "$t_g/\lambda$" on element gain patterns for different gap sizes ($t_g/\lambda=0$, 0.2, 0.4, and 0.5) for $k_o r_o=50$, $a/\lambda=0.43$, $b/\lambda=0.2$, $d/\lambda=0.5$, $t_d/\lambda=0.2$, $\varepsilon_r=2.56$, for $\theta=85°$ cuts. Patterns were combined in one figure, and for easy comparison, we added a 0.2 for $t_g/\lambda=0.2$ gain case, a 0.4 for the $t_g/\lambda=0.4$ case, and a 0.4 for the $t_g/\lambda=0.5$ case to separate their respective performances.



a) "Grating lobe" grid location in wave number plane for broadside ($v = 0$, $\zeta = 0$)



Fig. 5. Grating lobe diagram.
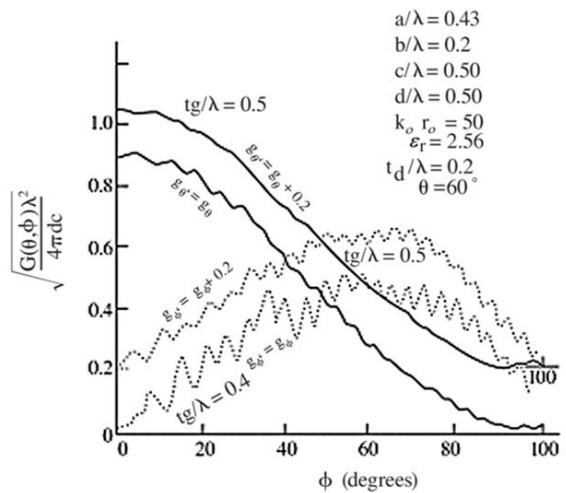


Fig. 7. Effect of air gap size "$t_g/\lambda$" on the element gain patterns for different gap sizes ($t_g/\lambda=0.4$, and 0.5) for $k_o r_o=50$, $a/\lambda=0.43$, $b/\lambda=0.2$, $d/\lambda=0.5$, $t_d/\lambda=0.2$, $\varepsilon_r=2.56$ for $\theta=60°$ cuts. Patterns were combined in one figure, and for easy comparison, we added a 0.2 for $t_g/\lambda=0.5$.

## B. Effect of radome thickness

For $t_d/\lambda = 0.3$ and $\theta = 60°$, Fig. 11 shows the element pattern for $t_g/\lambda = 0.2$ and a smooth element pattern for $t_g/\lambda = 0.5$. The latter case corresponds to the optimized geometry found in [l].
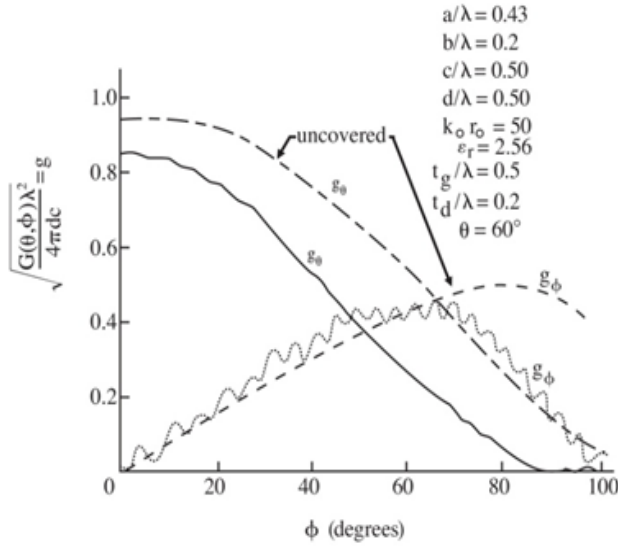


Fig. 8. Effect of air gap size "$t_g/\lambda$" on the element gain patterns relative to the uncovered case for $k_o r_o$=50, a/$\lambda$=0.43, b/$\lambda$=0.2, d/$\lambda$=0.5, $t_d/\lambda$=0.2, $\varepsilon_r$=2.56 for $\theta$=60° cuts.
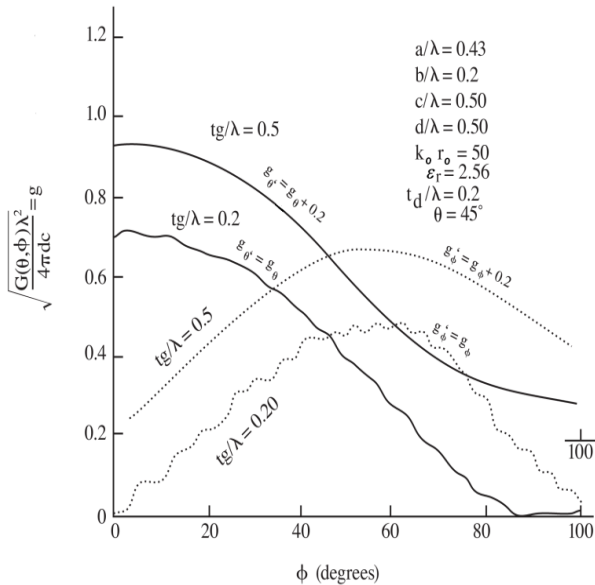


Fig. 9. Effect of air gap size "$t_g/\lambda$" on the element gain patterns for different gap sizes ($t_g/\lambda$=0.4, and 0.5) for $k_o r_o$=50, a/$\lambda$=0.43, b/$\lambda$=0.2, d/$\lambda$=0.5, $t_d/\lambda$=0.2, $\varepsilon_r$=2.56 for $\theta$=45° cuts.

## C. Effect of Radome Dielectric Constant $\varepsilon_r$

Figure 12 illustrates the situation for $\varepsilon_r = 4.05$ and $t_d/\lambda = 0.2$. In this case, the radome is no longer electrically thin, and in the absence of an air gap ($t_g = 0$), the principal H-plane $\theta = 90°$ exhibits a dip due to a TE surface wave. However, for $t_g/\lambda = 0.55$, the $\theta = 90°$ cut is acceptable. For $\theta = 60°$, $t_g/\lambda = 0.3$ gives rise to a rippled pattern, but $t_g/\lambda = 0.55$ is again sufficient to produce a smooth pattern (see Fig. 13).
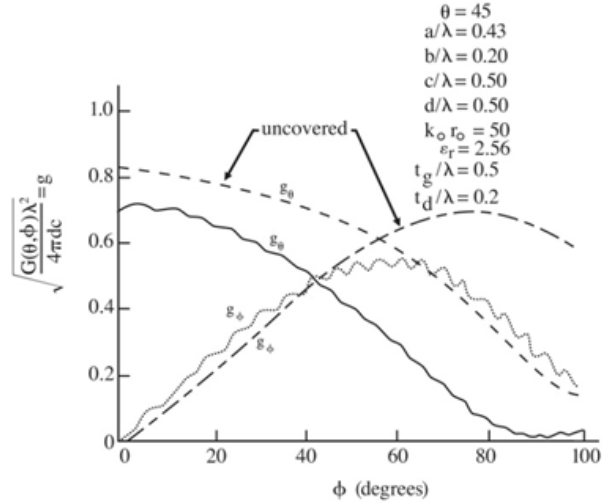


Fig. 10. Effect of air gap size "$t_g/\lambda$" on the element gain patterns relative to the uncovered case for $k_o r_o$=50, a/$\lambda$=0.43, b/$\lambda$=0.2, d/$\lambda$=0.5, $t_d/\lambda$=0.2, $\varepsilon_r$=2.56 for $\theta$=45° cuts.
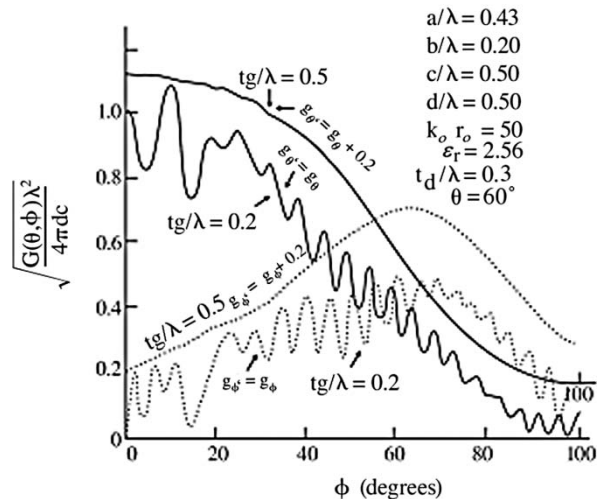


Fig. 11. Effect of air gap size "$t_g/\lambda$" on the element gain patterns for different gap sizes ($t_g/\lambda$=0.2, and 0.5) for $k_o r_o$=50, a/$\lambda$=0.43, b/$\lambda$=0.2, d/$\lambda$=0.5, $t_d/\lambda$=0.3, $\varepsilon_r$=2.56 for $\theta$=60° cuts. Patterns were combined in one figure, and for easy comparison, we added a 0.2 for $t_g/\lambda$=0.5.
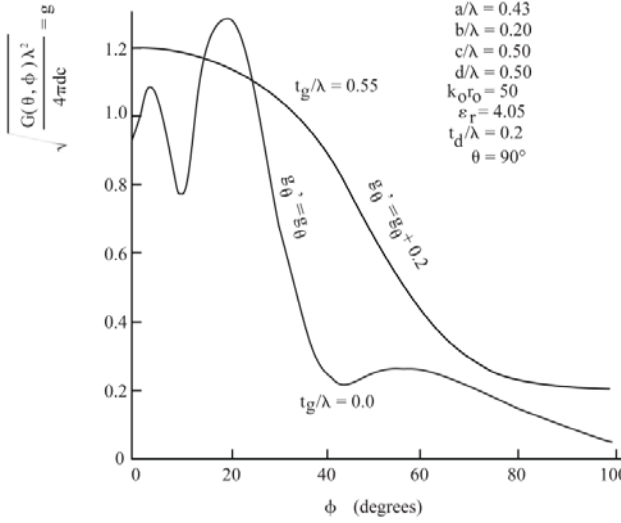
Fig. 12. Effect of air gap size "$t_g/\lambda$" on the element gain patterns for different gap sizes ($t_g/\lambda=0.0$, and 0.55) for $k_o r_o=50$, $a/\lambda=0.43$, $b/\lambda=0.2$, $d/\lambda=0.5$, $t_d/\lambda=0.2$, $\varepsilon_r=4.05$ for $\theta=90°$ cuts. Patterns were combined in one figure, and for easy comparison, we added a 0.2 for $t_g/\lambda=0.55$.
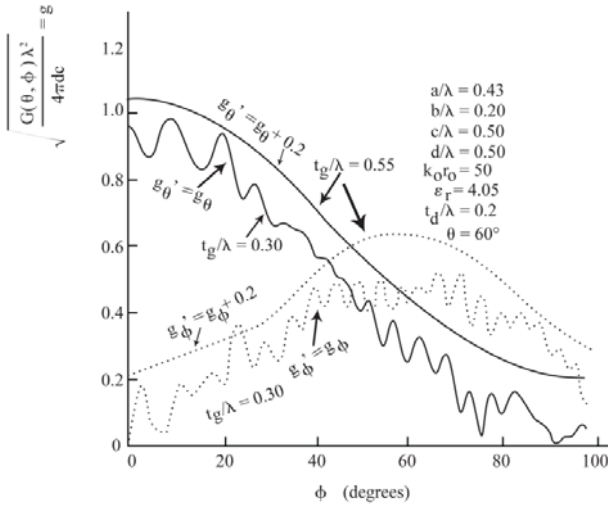


Fig. 13. Effect of air gap size "$t_g/\lambda$" on the element gain patterns for different gap sizes ($t_g/\lambda=0.3$, and 0.55) for $k_o r_o=50$, $a/\lambda=0.43$, $b/\lambda=0.2$, $d/\lambda=0.5$, $t_d/\lambda=0.2$, $\varepsilon_r=4.05$ for $\theta=60°$ cuts. Patterns were combined in one figure, and for easy comparison, we added a 0.2 for $t_g/\lambda=0.55$.

## V. CONCLUSION

This paper extends the ideas of [l] for shaping the element patterns of conformal arrays scanning in two planes in the presence of a near field, dielectric radome. The spacing is not smaller than 0.5 $\lambda$, and the compensation is accomplished by an adjustable air gap. The gap compensation method works fairly well. The axial scan is limited by the E-plane dip, which can be predicted

from the planar surface wave dispersion curves. Axial polarization allows further scanning along the axis as compared to that of the circumferential polarization which is limited by the H-plane dip that is closer to broadside to that of the axial case. However, cross-polarization is the main problem for axially polarized excitation and is present off the principal planes even without the radome. From the data shown, it appears that the cross-polarization slightly worsens in the presence of a radome. For a sufficiently large departure from the principal planes, the cross polarization level exceeds that of the principal polarization even in the lit region, limiting the extent of the excited arc in an active array and the extent of additional phase scanning in the azimuthal direction. This polarization is more suitable for applications where the desired scan sector is larger in the axial direction than in the circumferential direction

## APPENDIX

### A. Radial Transmission Line

In view of equation (9), $i''_{v_m,\varsigma_n}$ and $v'_{v_m,\varsigma_n}$ satisfy the Bessel's differential equation and therefore one has the following expressions for the radial modal transmission line in the $i\underline{th}$ layer (see Fig. l),

$$V'_{v_m,\varsigma_n}(\rho) =$$
$$V'^{(+i)}_{v_m,\varsigma_n} H^{(2)}_{v_m}(\kappa_{ni}\rho) + V'^{(-i)}_{v_m,\varsigma_n} H^{(1)}_{v_m}(\kappa_{ni}\rho)$$

$$V''_{v_m,\varsigma_n}(\rho) =$$
$$Z''_{ni}\{I''^{(+i)}_{v_m,\varsigma_n} H^{(2)'}_{v_m}(\kappa_{ni}\rho) + I''^{(-i)}_{v_m,\varsigma_n} H^{(1)'}_{v_m}(\kappa_{ni}\rho)\}$$

$$I'_{v_m,\varsigma_n}(\rho) =$$
$$Y'_{ni}\{V'^{(+i)}_{v_m,\varsigma_n} H^{(2)'}_{v_m}(\kappa_{ni}\rho) + V'^{(-i)}_{v_m,\varsigma_n} H^{(1)'}_{v_m}(\kappa_{ni}\rho)\}$$

$$I''_{v_m,\varsigma_n}(\rho) =$$
$$\{I''^{(+i)}_{v_m,\varsigma_n} H^{(2)}_{v_m}(\kappa_{ni}\rho) + I''^{(-i)}_{v_m,\varsigma_n} H^{(1)}_{v_m}(\kappa_{ni}\rho)\},$$

where $Y'_{ni} = \dfrac{j\omega\varepsilon_i}{\kappa_{ni}}$; and $Z''_{ni} = \dfrac{j\omega\mu_o}{\kappa_{ni}}$ . (A1.1)

But, for i=3 and $\rho \geq \rho_2$, we have only forward traveling waves,

$$V''_{v_m,\varsigma_n}(\rho^+) = I''^{(+3)}_{v_m,\varsigma_n} Z''_{n3} H^{(2)'}_{v_m}(\kappa_{n3}\rho)$$
$$I''_{v_m,\varsigma_n}(\rho^+) = I''^{(+3)}_{v_m,\varsigma_n} H^{(2)}_{v_m}(\kappa_{n3}\rho)$$
$$V'_{v_m,\varsigma_n}(\rho^+) = V'^{(+3)}_{v_m,\varsigma_n} H^{(2)}_{v_m}(\kappa_{n3}\rho)$$
$$I'_{v_m,\varsigma_n}(\rho^+) = V'^{(+3)}_{v_m,\varsigma_n} Y'_{n3} H^{(2)'}_{v_m}(\kappa_{n3}\rho)$$

(A1.2)

where $\kappa_{n3} = \kappa_{n1}$ and $Z_{n3} = Z_{n1}$, and $H_n^{(1,2)}(x)$ denotes the Hankel function of the first or second type with argument x and order n.

## B. Transmission Matrix $T_{12}$

The various voltages and currents in the *i*-layer at $\rho_{i-1}^+$ can be related to those at $\rho_i^-$ using the following transmission representation,

$$\begin{bmatrix} V_{v_m,\varsigma_n}^{''}(\rho_{i-1}^+) \\ I_{v_m,\varsigma_n}^{''}(\rho_{i-1}^+) \\ V_{v_m,\varsigma_n}^{'}(\rho_{i-1}^+) \\ I_{v_m,\varsigma_n}^{'}(\rho_{i-1}^+) \end{bmatrix} = [ABCD_i] \begin{bmatrix} V_{v_m,\varsigma_n}^{''}(\rho_i^-) \\ I_{v_m,\varsigma_n}^{''}(\rho_i^-) \\ V_{v_m,\varsigma_n}^{'}(\rho_i^-) \\ I_{v_m,\varsigma_n}^{'}(\rho_i^-) \end{bmatrix} \quad \text{(B1.1)}$$

$$[ABCD_i] = \begin{bmatrix} A_i^{''} & B_i^{''} & 0 & 0 \\ C_i^{''} & D_i^{''} & 0 & 0 \\ 0 & 0 & A_i^{'} & B_i^{'} \\ 0 & 0 & C_i^{'} & D_i^{'} \end{bmatrix} \quad \text{(B1.2)}$$

and

$$A_i^{''} = \frac{Z_{ni}^{''}}{\Delta_i^{''}}[H_{v_m}^{(2)'}(\kappa_{ni}\rho_{i-1})H_{v_m}^{(1)}(\kappa_{ni}\rho_i)$$

$$-H_{v_m}^{(1)'}(\kappa_{n,i}\rho_{i-1})H_{v_m}^{(2)}(\kappa_{n,i}\rho_{i-1})]$$

$$B_i^{''} = \frac{Z_{ni}^{''}Z_{ni}^{''}}{\Delta_i^{''}}[H_{v_m}^{(2)'}(\kappa_{ni}\rho_{i-1})H_{v_m}^{(1)'}(\kappa_{ni}\rho_i)$$

$$-H_{v_m}^{(1)'}(\kappa_{ni}\rho_{i-1})H_{v_m}^{(2)'}(\kappa_{ni}\rho_i)]$$

$$C_i^{''} = \frac{1}{\Delta_i^{''}}[H_{v_m}^{(2)}(\kappa_{ni}\rho_{i-1})H_{v_m}^{(1)}(\kappa_{ni}\rho_i)$$ \quad \text{(B1.3)}

$$-H_{v_m}^{(1)}(\kappa_n\rho_{i-1})H_{v_m}^{(2)}(\kappa_{ni}\rho_i)]$$

$$D_i^{''} = \frac{Z_{ni}^{''}}{\Delta_i^{''}}[H_{v_m}^{(2)}(\kappa_{ni}\rho_{i-1})H_{v_m}^{(1)'}(\kappa_{ni}\rho_i)$$

$$-H_{v_m}^{(1)}(\kappa_n\rho_{i-1})H_{v_m}^{(2)'}(\kappa_{ni}\rho_i)]$$

where $\Delta_2^{''}$ is given by,

$$\Delta_i^{''} = -Z_{ni}^{''}[H_{v_m}^{(2)'}(\kappa_{ni}\rho_i)H_{v_m}^{(1)}(\kappa_{ni}\rho_i)$$

$$-H_{v_m}^{(2)}(\kappa_{ni}\rho_i)H_{v_m}^{(1)'}(\kappa_{ni}\rho_i)] = \frac{4j}{\pi\kappa_{ni}\rho_i}Z_{ni}^{''} \quad \text{(B1.4)}$$

And similarly $A_i^{'}$, $B_i^{'}$, $C_i^{'}$, and $D_i^{'}$ are deduced by first dividing all the above terms for the (``) case by $(Z_{ni}^{''}Z_{ni}^{''})$ and then utilizing the following substitution,

$(H_{v_m}^{(1,2)'}(\kappa_{ni}\rho_{1,2}^+), H_{v_m}^{(1,2)}(\kappa_{ni}\rho_{1,2}^+), ``)$

$\rightarrow(H_{v_m}^{(1,2)'}(\kappa_{n2}\rho_{1,2}^+), H_{v_m}^{(1,2)}(\kappa_{ni}\rho_{1,2}^+), `)$

As an example $A_i^{'}$ is given by,

$$A_i^{'} = \frac{Y_{ni}^{'}}{\Delta_i^{'}}[H_{v_m}^{(2)}(\kappa_{ni}\rho_{i-1})H_{v_m}^{(1)'}(\kappa_{ni}\rho_i)$$ \quad \text{(B1.5)}

$$-H_{v_m}^{(1)}(\kappa_{ni}\rho_{i-1})H_{v_m}^{(2)'}(\kappa_{ni}\rho_i)]$$

where $\Delta_2^{'}$ is given by,

$$\Delta_i^{'} = -Z_{ni}^{'}[H_{v_m}^{(2)'}(\kappa_{ni}\rho_i)H_{v_m}^{(1)}(\kappa_{ni}\rho_i)$$

$$-H_{v_m}^{(2)}(\kappa_{ni}\rho_i)H_{v_m}^{(1)'}(\kappa_{ni}\rho_i)] = \frac{4j}{\pi\kappa_{ni}\rho_i}Z_{ni}^{'} \quad \text{(B1.6)}$$

## C. Boundary Conditions and The Coupling Matrix $P^{i,i+1}$

In view of the continuity of $E_{z_{v_m,\varsigma_n}}$ and $H_{z_{v_m,\varsigma_n}}$ at both $\rho_1$ and $\rho_2$ as well as the continuity of $e_{z_{v_m,\varsigma_n}}^{'}$ across the dielectric interface at both $\rho=\rho_1$ and $\rho_2$, the total voltages and currents must be continuous at both $\rho_2$ and $\rho_1$ i.e.

$$V_{v_m,\varsigma_n}^{'}(\rho_{1,2}^+) = V_{v_m,\varsigma_n}^{'}(\rho_{1,2}^-)$$

$$I_{v_m,\varsigma_n}^{''}(\rho_{1,2}^+) = I_{v_m,\varsigma_n}^{''}(\rho_{1,2}^-) \quad \text{(C1.1)}$$

On the other hand, the continuity of $E_\Phi$ and $H_\Phi$ at $\rho_1$ and $\rho_2$ yields via equations (2), (3) and (9) the following,

$$\begin{bmatrix} V_{v_m,\varsigma_n}^{''}(\rho_i^-) \\ I_{v_m,\varsigma_n}^{''}(\rho_i^-) \\ V_{v_m,\varsigma_n}^{'}(\rho_i^-) \\ I_{v_m,\varsigma_n}^{'}(\rho_i^-) \end{bmatrix} = P^{i,i+1} \begin{bmatrix} V_{v_m,\varsigma_n}^{''}(\rho_i^+) \\ I_{v_m,\varsigma_n}^{''}(\rho_i^+) \\ V_{v_m,\varsigma_n}^{'}(\rho_i^+) \\ I_{v_m,\varsigma_n}^{'}(\rho_i^+) \end{bmatrix} \quad \text{(C1.2)}$$

The coupling matrix $P^{i,i+1}$ is given by,

$$P^{i,i+1} = \begin{bmatrix} 1 & 0 & X_{mn}^{i,i+1}/\rho_i & 0 \\ 0 & 1 & 0 & 0 \\ 0 & 0 & 1 & 0 \\ 0 & -X_{mn}^{i,i+1}/\rho_i & 0 & 1 \end{bmatrix} \quad \text{(C1.3)}$$

where

$$X_{mn}^{i,i+1} = v_m\varsigma_n(\frac{1}{\kappa_{ni}^2} - \frac{1}{\kappa_{ni+1}^2}) \quad \text{(C1.4)}$$

Repeating for $i$=1 and $i$=2, we can find the overall transmission from $\rho_0^+$ to $\rho_2^-$ given by,

$$\begin{bmatrix} V_{\nu_m,\varsigma_n}^{''}(\rho_0^+) \\ I_{\nu_m,\varsigma_n}^{''}(\rho_0^+) \\ V_{\nu_m,\varsigma_n}^{'}(\rho_0^+) \\ I_{\nu_m,\varsigma_n}^{'}(\rho_0^+) \end{bmatrix} = \begin{bmatrix} T_{12} \end{bmatrix} \begin{bmatrix} V_{\nu_m,\varsigma_n}^{''}(\rho_2^-) \\ I_{\nu_m,\varsigma_n}^{''}(\rho_2^-) \\ V_{\nu_m,\varsigma_n}^{'}(\rho_2^-) \\ I_{\nu_m,\varsigma_n}^{'}(\rho_2^-) \end{bmatrix} \quad \text{(C1.5)}$$

$$= \begin{bmatrix} T_{12} \end{bmatrix} \begin{bmatrix} I_{\nu_m,\varsigma_n}^{''(+3)} Z_{n3}^{''} H_{\nu_m}^{(2)'}(\kappa_{n3}\rho_2^+) \\ I_{\nu_m,\varsigma_n}^{''(+3)} H_{\nu_m}^{(2)}(\kappa_{n3}\rho_2^+) \\ V_{\nu_m,\varsigma_n}^{'(+3)} H_{\nu_m}^{(2)}(\kappa_{n3}\rho_2^+) \\ V_{\nu_m,\varsigma_n}^{'(+3)} Y_{n3}^{'} H_{\nu_m}^{(2)'}(\kappa_{n3}\rho_2^+) \end{bmatrix}$$

where

$$T_{12} = \begin{bmatrix} ABCD_1 \end{bmatrix} P_{12} \begin{bmatrix} ABCD_2 \end{bmatrix} P_{23}. \quad \text{(C1.6)}$$

Repeating for i=1 and i=2, we can find the overall transmission from $\rho_0^+$ to $\rho_2^-$ given by,

$$\begin{bmatrix} V_{\nu_m,\varsigma_n}^{''}(\rho_0^+) \\ I_{\nu_m,\varsigma_n}^{''}(\rho_0^+) \\ V_{\nu_m,\varsigma_n}^{'}(\rho_0^+) \\ I_{\nu_m,\varsigma_n}^{'}(\rho_0^+) \end{bmatrix} = \begin{bmatrix} T_{12} \end{bmatrix} \begin{bmatrix} V_{\nu_m,\varsigma_n}^{''}(\rho_2^-) \\ I_{\nu_m,\varsigma_n}^{''}(\rho_2^-) \\ V_{\nu_m,\varsigma_n}^{'}(\rho_2^-) \\ I_{\nu_m,\varsigma_n}^{'}(\rho_2^-) \end{bmatrix} \quad \text{(C1.7)}$$

$$= \begin{bmatrix} T_{12} \end{bmatrix} \begin{bmatrix} I_{\nu_m,\varsigma_n}^{''(+3)} Z_{n3}^{''} H_{\nu_m}^{(2)'}(\kappa_{n3}\rho_2^+) \\ I_{\nu_m,\varsigma_n}^{''(+3)} H_{\nu_m}^{(2)}(\kappa_{n3}\rho_2^+) \\ V_{\nu_m,\varsigma_n}^{'(+3)} H_{\nu_m}^{(2)}(\kappa_{n3}\rho_2^+) \\ V_{\nu_m,\varsigma_n}^{'(+3)} Y_{n3}^{'} H_{\nu_m}^{(2)'}(\kappa_{n3}\rho_2^+) \end{bmatrix}$$

where

$$T_{12} = \begin{bmatrix} ABCD_1 \end{bmatrix} P_{12} \begin{bmatrix} ABCD_2 \end{bmatrix} P_{23}. \quad \text{(C1.8)}$$

### REFERENCES

[1] A. Fathy and A. Hessel, "Element pattern approach to design of dielectric windows for conformal phased arrays," *IEEE Trans. Ant. Prop.*, vol. 32, no. 1, Jan. 1984.

[2] A. E. Fathy, "Design of a near field protective dielectric radome "window" for a curved phased array antenna-circumferential polarization case," *IEEE Trans. Prop.*, vol. 54, no. 11, pp. 3356-3366, Nov. 2006.

[3] A. Hessel, "Mutual coupling effects in circular arrays on cylindrical surfaces - aperture design implications and analysis in phased array antennas,"A. *Oliner and G. Knittel, Eds.* , p. 273, April 1972.

[4] A. Fathy and A. Hessel, "Wave contributions to the element pattern of a cylindrical array surrounded by a dielectric radome," *URSI Symposium Digest (Houston, Texas)*, pp. 98, 1983.

[5] D. T. Mc. Grath, and V. P. Pyati, "Phased array antenna analysis with the hybrid finite element method," *IEEE Transactions on Antennas and Propagation*, vol. 42, pp. 1625-1630, Dec. 1994.

[6] D. T. McGrath, "Accelerated periodic hybrid finite element method for integrated array element and radome design," *Phased Array Systems and Technology, 2000. Proceedings*, pp.319-322, 2000.

**Aly E. Fathy** (S'82-M'84-SM'92-F'04) received the B.S.E.E. degree, the B.S. degree in pure and applied mathematics, and the M.S.E.E. degree from Ain Shams University, Cairo, Egypt, in 1975, 1979, and 1980, respectively, and the Ph.D. degree from the Polytechnic Institute of New York, Brooklyn, in 1984. In February 1985, he joined the RCA Research Laboratory (currently the Sarnoff Corporation), Princeton, NJ, as a Member of the Technical Staff. In 2001, he was promoted to a Senior Member of the Technical Staff. At Sarnoff, he has been engaged in the research and development of various enabling technologies such as high-$T_c$ superconductors, LTCC, and reconfigurable holographic antennas. He was also an Adjunct Professor at the Cooper Union School of Engineering, New York, NY. In August 2003, he joined the University of Tennessee, Knoxville, as an Associate Professor and his current research interests include wireless reconfigurable antennas, see thru walls, ultra wide band systems, and high efficiency high linearity combining of digital signals for base station amplifiers. He has developed various microwave components/subsystems such as holographic reconfigurable antennas, radial combiners, direct broadcast antennas (DBS), speed sensors, and low-temperature co-fired ceramic packages for mixed-signal applications. He holds eleven U.S. patents, and has published numerous transaction and conference papers. He is sponsored by different companies and international research labs including Intel Corp, Rockwell Collins, Winegard Company, Oak Ridge National Lab, Sarnoff Lab, and Y12. Dr. Fathy is an IEEE fellow, a member of Sigma Xi, and Eta Kappa Nu. He was the recipient of five Sarnoff Outstanding Achievement Awards (1988, 1994,1995,1997, 1999). He is an active member of the IEEE MTT-S International Microwave Symposium (IMS) Technical Program Committee, and the IEEE radio and wireless steering Committee. He is currently the Chair of the 2008 IEEE radio and wireless conference.